BNL-226179-2024-JAAM

Unraveling the Formation Mechanisms of Highly Oriented Tin Perovskite with a 3D-over-2D Heterostructure

Y. Xu, Y. Zhang

To be published in "ACS Energy Letters"

September 2024

Center for Functional Nanomaterials

Brookhaven National Laboratory

U.S. Department of Energy

USDOE Office of Science (SC), Basic Energy Sciences (BES). Scientific User Facilities (SUF)

DISCLAIMER

Unraveling the Formation Mechanisms of Highly Oriented Tin Perovskite with a 3D-over-2D Heterostructure

Yuanze Xu[1], Juno Kim[2], Shripathi Ramakrishnan[1], Taiyi Chen[1], Xiaoyu Zhang[1], Yugang Zhang[3], Andrew J. Musser[2] and Qiuming Yu[*1]

[1]Robert Frederick Smith School of Chemical and Biomolecular Engineering, Cornell University, Ithaca, New York 14853, United States

[2]Department of Chemistry and Chemical Biology, Cornell University, Ithaca, New York 14853, United States

[3]Center for Functional Nanomaterials, Brookhaven National Laboratory, Upton, New York 11973, United States

Email: qy10@cornell.edu

Abstract

Tin-based perovskite (TinPVK) has become the most promising candidate to lead-free perovskite solar cells, owing to its low toxicity and improved photovoltaic performance. However, due to the absence of 4f shell, TinPVKs suffer from uncontrolled crystallization, limiting the power conversion efficiency (PCE) of tin perovskite solar cells (TinPSCs). Here, we systematically study the ligand regulated crystallization process of TinPVK. We find that with elongated spin time, TinPVK crystals undergo reorientation and lateral growth. 3D α-phase $FASnI_3$, 2D (n = 2) and 2D (n = 1) phases emerge sequentially to form a '3D-over-2D' heterostructure via a proposed 'diffusion-propagation' mechanism. TinPSCs exhibit improved open circuit voltage (V_{OC}) due to favorable energy level alignment of the '3D-over-2D' heterostructure, with a champion PCE of 13.07% and T_{80} over 1200 hours. This work provides mechanistic insights on controlled crystallization and heterostructure formation of TinPVKs, paving the way towards high efficiency TinPSCs.

TOC Graphic

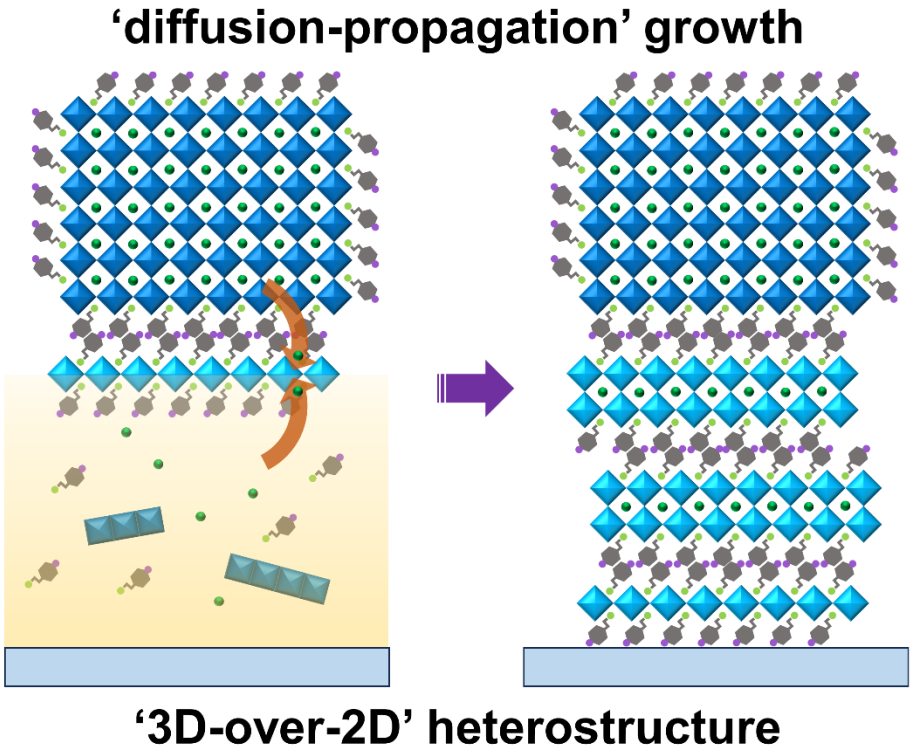

Perovskite solar cells have achieved impressive progress on both the power conversion efficiency (PCE) and long-term stability over the past decade.[1-3] However, the high toxicity of water-soluble lead ions is a considerable threat to both human health and aquatic environments, and therefore remains a significant concern towards the commercialization of perovskite solar cells.[4-6] Although encapsulation, absorption, and recycling of lead-containing perovskite materials might alleviate lead leakage,[7-9] replacing lead with non-toxic elements is an ultimate way to solve this issue. Tin-based perovskite solar cells (TinPSCs) have emerged as one of the most promising alternatives for the low toxicity, earth abundance, suitable bandgap, and high carrier mobility.[10-12] Up to date, the PCE of TinPSCs still lag behind their lead-based counterparts. Tin-based perovskites (TinPVKs) suffer from easy oxidation from Sn^{2+} to Sn^{4+}, causing excessive p-doping and reducing the device performance. The $4s^2$ electrons can be easily removed due to the absence of 4f shell as compared to Pb.[13-14] Moreover, TinPVKs undergo fast crystallization because of the high Lewis acidity of Sn^{2+}, leading to high defect density and random grain orientations in TinPVK films.[12,15] Therefore, deeper understandings on how to control the crystallization processes of TinPVKs are urgently needed to construct efficient TinPSCs.

Incorporation of organic ligands in perovskite precursors is one major strategy to control the crystallization of TinPVKs and has demonstrated PCE over 15%.[16-17] The ligands bond dynamically to TinPVK grain surfaces during the crystallization process, leading to reduced defect density and shifted band structures of the TinPVK films.[18-21] In addition, the ligands can also participate in the formation of two-dimensional (2D) TinPVK phases. For example, phenethylammonium iodide (PEAI), when mixed in precursors, can promote the formation of mixed 2D and 3D TinPVK phases, which simultaneously enhance the open circuit voltage (V_{OC}) and improve the device stability.[22-24] While the strong bonding between the ligands and 3D TinPVK lattice plays an important role in regulating the crystallization, the interactions between the ligands can also significantly change the crystallization scheme. 4-fluorophenethylammonium iodide (4-FPEAI), due to the interactions between the fluorine atom and the π-ring, tend to adopt a 'slip-on' packing mode when forming 2D perovskite or attaching to 3D perovskite grain surfaces.[25-26] The compact packing shortens the interlayer spacing between the 2D perovskite sheets, hence enhancing the charge transport across the out-of-plane direction.[27]

In this work, we systematically study the ligand-assisted crystallization processes of TinPVK with a suite of in-situ and ex-situ techniques. Specifically, PEAI and 4-FPEAI are blended into TinPVK precursors to both regulate the crystallization and form 2D/3D heterostructures. We find that rather than random crystal growth with PEAI, 4-FPEAI leads to the growth of highly oriented TinPVK grains with their {100} facets exposed parallel to substrates. The PEAI films show no 2D components during spin coating and form '2D-3D-mix' heterostructures after annealing. In contrast, 4-FPEAI promotes the growth of 2D phases at the bottom of the TinPVK films, following a proposed 'diffusion-propagation' mechanism which results in a '3D-over-2D' heterostructure. The '3D-over-2D' heterostructure removes the barrier for electron transport across the TinPVK/ETL interface,[28] while impose little barrier for hole transport across the TinPVK/HTL interface due to little energy level mismatch between the valence band maxima (VBM) of 3D and 2D phases. As a result, the champion 4-FPEAI TinPSC achieves a PCE of 13.07% and a high V_{OC} of 0.94 V, surpassing the PEAI TinPSC with a PCE of 9.69% and a V_{OC} of 0.76 V.

We fabricated the TinPVK films with a formula of $A'_{0.1}FA_{0.9}SnI_3$ (A' = PEA or 4-FPEA) using a one-step spin coating method. Due to the high Lewis acidity of SnI_2, the crystallization of 3D α-phase $FASnI_3$ requires much lower energy than their lead-counterparts.[10] This allows TinPVK to partially crystallize even at room temperature by the expulsion of solvents (DMF:DMSO, v:v = 4:1), manifested by the darkening of film color during the spin coating processes (**Figure 1a**). An intermediate step, such as vacuuming or heating under a mild temperature,[28-29] has been demonstrated to grow high quality TinPVK films. Similarly, we observe film color darkening when we leave the TinPVK films to spin for longer duration after injecting the toluene as the antisolvent (**Figure 1b**), which indicates a pre-crystallization stage. To study the impact of spin time on the crystal structure of TinPVKs, we coated TinPVK films with the same spin speed ramping program and a fixed antisolvent injection timing but leave the films to continue spinning for different durations at the second spin stage (**Figure 1c**). During the elongated spin stage, along with the pre-crystallization of TinPVK films, the unevaporated solvents in the film can facilitate the diffusion of ions and may lead to the evolution of TinPVK heterostructures.[30] Here, we note the samples by the spin time after the antisolvent injection. As shown in **Figure 1d**, the 10 s PEAI film covers most of the substrate with only a few pinholes. The pinholes are eliminated in the 40 s PEAI film, with no significant changes in the film roughness and grain sizes. However, the 70 s PEAI film shows both increased roughness and reduced grain sizes, possibly resulting from the redissolution and regrowth aided by the remaining solvent. In contrast, the 10 s 4-FPEAI film exhibits rectangular grain morphology, with smooth grain surfaces, high surface roughness and incomplete film coverage (**Figure 1e**). Owing to the 'slip-on' packing mode of 4-FPEA ligands, they attach firmly and preferably to the {100} facet of 3D TinPVK grain surfaces. This strong attachment retards the crystal growth along the (100) plane, resulting in {100} facet capped grains. With 40 s spin time, the 4-FPEAI film develops into a smooth and compact film with significantly improved surface coverage, suggesting a slow lateral growth aided by the remaining solvent. The elimination of pinholes will suppress shunt channels and is ideal for planar solar cells. With a longer spin time of 70 s, the 4-FPEAI film remains mostly unchanged in surface morphology. The changes in surface morphology suggest that crystal growth is slower with 4-FPEAI than with PEAI in precursor, and the elongated spin time promotes lateral growth towards full surface coverage.

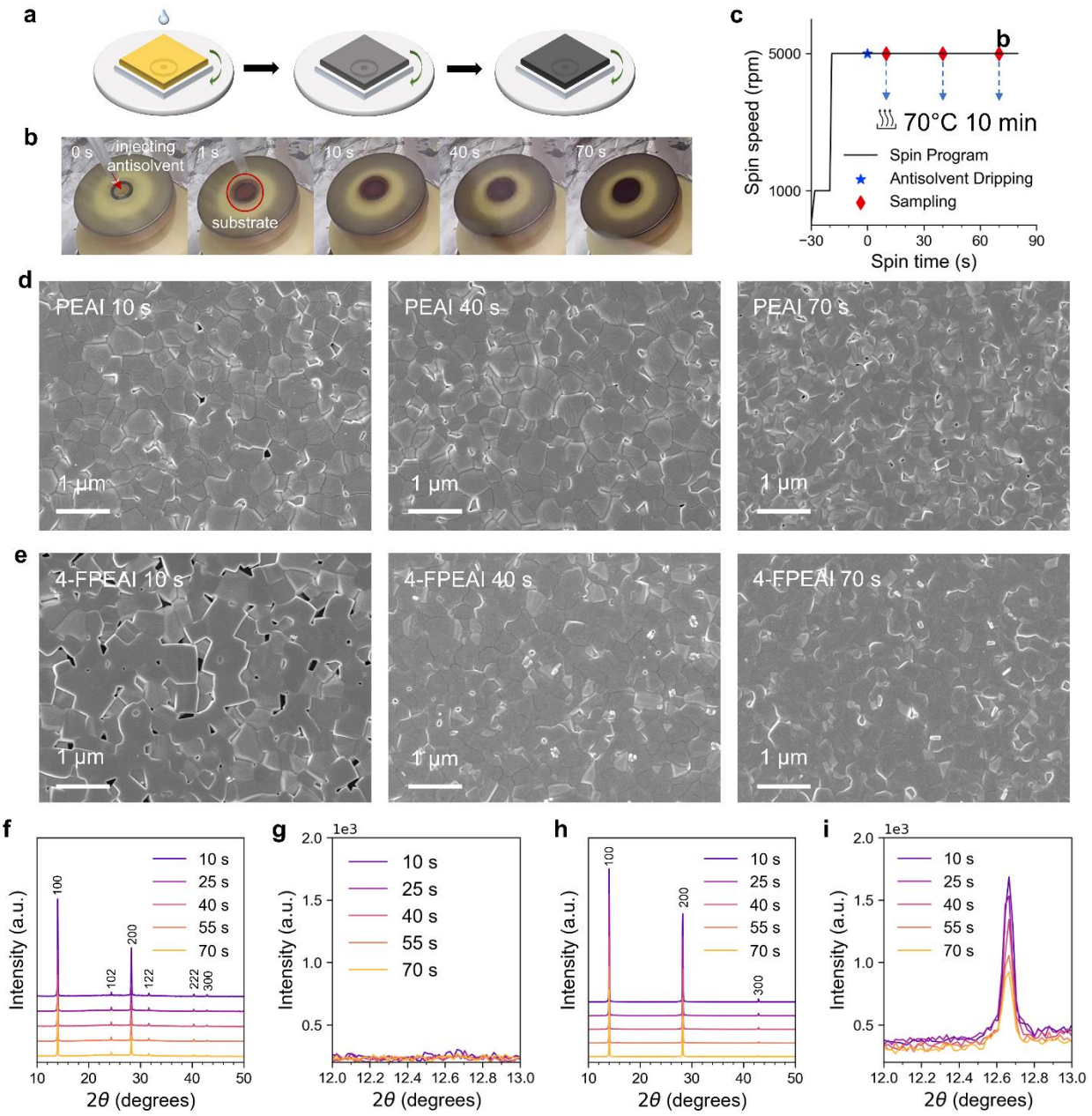

Figure 1. Crystal structure and film morphology of tin perovskites with different spin time.
(a) Schematic illustration of film color change during a typical TinPVK spin coating process. (b) Photographic images of a spinning TinPVK film during a typical spin coating process. (c) The spin program used for the fabrication of TinPVK films. Top-view SEM images of the film morphology change over spin times with (d) PEAI and (e) 4-FPEAI as ligands. (f) XRD spectra of TinPVK films at different spin time with PEAI as ligands and (g) zoom-in spectra to indicate the evolution of SnI_2 species. (h) XRD spectra of TinPVK films at different spin time with 4-FPEAI as ligands and (i) zoom-in spectra to indicate the evolution of SnI_2 species. All films are annealed at 70°C for 10 min after spin coating.

We further explored the changes in TinPVK microstructures with different spin times by taking the X-ray diffraction (XRD) patterns. The PEAI films show XRD peaks from multiple crystallographic planes of the

3D α-phase $FASnI_3$, (102), (122), (222) and (h00), indicating random crystal orientations (**Figure 1f**). The films show no SnI_2 peak at 2θ = 12.7° for all different spin times (**Figure 1g**), [31] suggesting a fast crystallization of TinPVKs at the consumption of precursors upon injecting the antisolvent. PEAI has no preference on which crystal facet it attaches to, and therefore exhibits a relatively weak effect on retarding TinPVK crystallization. In contrast, the XRD patterns of 4-FPEAI films are predominantly by peaks from (h00) planes, indicating a dominant orientation of (100) plane facing upwards (**Figure 1h**). This agrees with the observed crystal morphology. Unlike the PEAI films, the 4-FPEAI films show SnI_2 peak descending with longer spin time (**Figure 1i**), indicating a slow crystallization step of TinPVKs. Since the 4-FPEA ligands attach preferably on the {100} facets with a compact coverage, stoichiometrically rich SnI_2 composition cannot attach to crystal grains, but only forming isolated small domains and exhibiting signals in XRD patterns. However, in the case of PEAI, as the PEA ligands attach randomly to crystal planes with a relatively sparse coverage, SnI_2 can attach to grain surfaces and therefore show weak, unresolvable peaks. Besides, the (100) peak of 3D α-phase $FASnI_3$ decreases in intensity and increases in FWHM over spin time for both PEAI and 4-FPEAI films (**Figure S1**). The increased FWHM originates from wider grain size distribution caused by the redissolution of large grains and emergence of small grains. In light of these results, we find that compared with PEAI as ligands, the 3D α-phase $FASnI_3$ grows significantly slower with 4-FPEAI. The strong binding of 4-FPEA ligands preferably on the (100) plane leads to {100} facet capped rectangular grains. The packed 4-FPEA ligands also induce favorable interactions between the facets, promoting highly oriented TinPVK films with the {100} facet facing perpendicularly upwards to the substrate. Moreover, although the nucleation and growth triggered by antisolvent consume most of the precursor, 4-FPEAI prevents the films from depleting the SnI_2 precursor. The SnI_2 left in the film then supplies slow lateral growth, and therefore insufficient spin time limits the lateral growth and results in gaps between grains as observed in the 10 s 4-FPEAI film. Continuous lateral growth of the existing grains merges the gaps as shown in the 40 s and 70 s 4-FPEAI films. In contrast, the fast crystallization in the PEAI films completely consumes the SnI_2 precursor shortly after injecting the antisolvent, and a longer spin time can only cause redissolution and regrowth of TinPVK crystals.

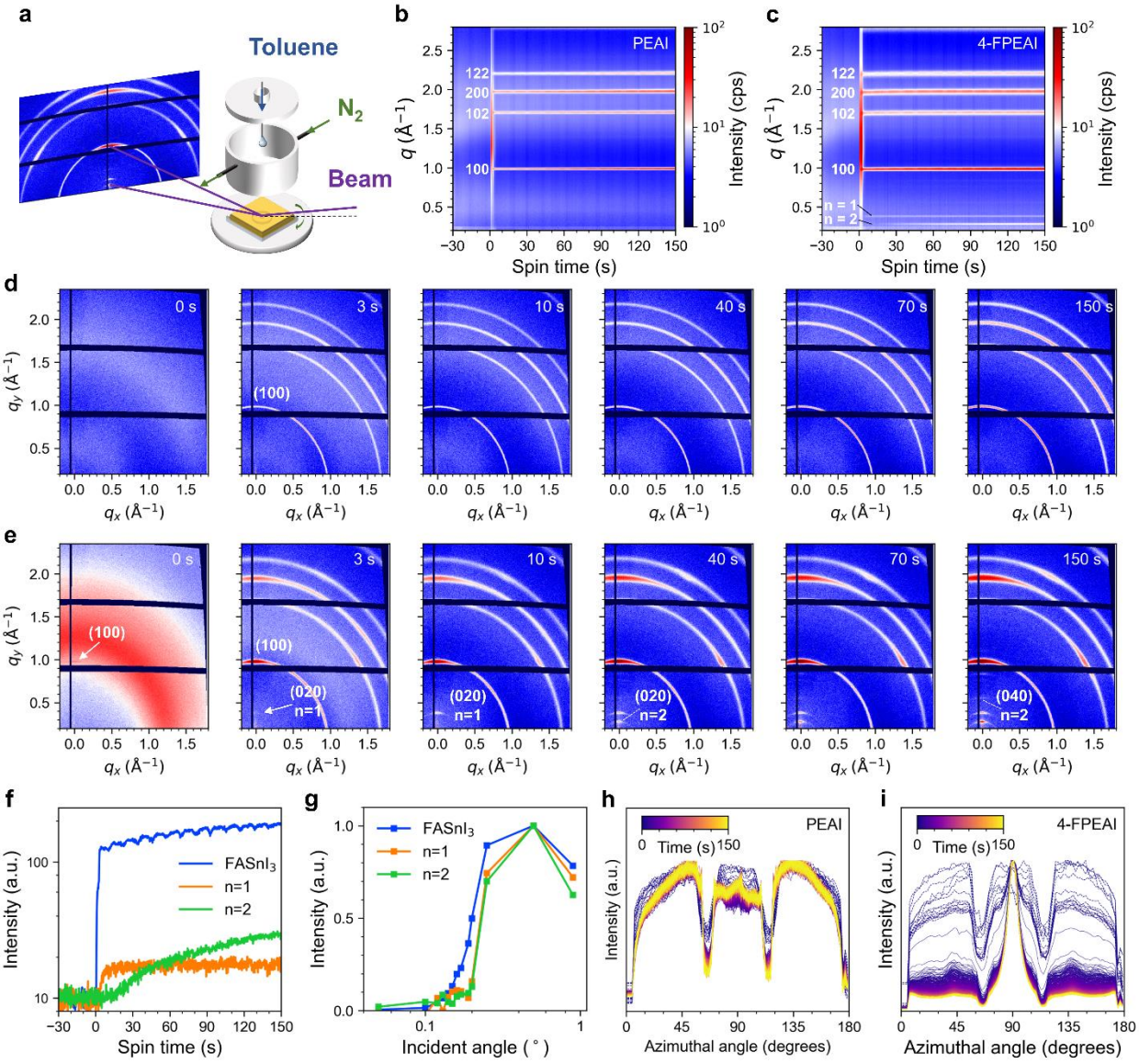

Figure 2. Crystal structure evolution of tin perovskites during spin coating.
(a) Schematic illustration of the in-situ GIWAXS setup. Evolutions of circularly averaged in-situ GIWAXS linecuts during the spin coating of TinPVK films with (b) PEAI and (c) 4-FPEAI as ligands. GIWAXS heatmap frames during the spin coating processes of (d) PEAI and (e) 4-FPEAI films. Time zero is set to the antisolvent injection moment. (f) Temporal evolution of peak intensities corresponding to 3D and 2D (n = 1 and n = 2) phases in the 4-FPEAI film. (g) Incident angle dependent peak intensities corresponding to 3D and 2D (n = 1 and n = 2) phases in the 4-FPEAI film at the end of spin coating. Evolutions of azimuthal angle dependent peak intensities of the 3D α-phase $FASnI_3$ (100) peak in the (h) PEAI and (i) 4-FPEAI films.

To gain a deeper understanding of the crystallization processes of TinPVKs with PEAI and 4-FPEAI ligands, we conducted in-situ grazing-incidence wide-angle X-ray scattering (GIWAXS) measurements. We enclosed the samples in an N_2-flowed chamber during the measurements to exclude the effect of Sn^{2+} oxidation (**Figure 2a**). A detailed setup is depicted in **Figure S2**. We followed the same spin speed ramping program as the fabrication of TinPVK films, with the same antisolvent injection timing. The incident angle α was

kept at 0.9° to collect GIWAXS data from the whole depth of the films. To catch the rapid changes in crystal microstructures, we used a short exposure time of 0.2 s, which resulted in lower intensity but higher time resolution. Heatmaps of the circularly averaged in-situ GIWAXS linecuts are displayed in **Figure 2b-c** for the spin coating processes with PEAI and 4-FPEAI, respectively. At time zero, when the antisolvent hits the substrate, there is a wide peak between q = 1 $Å^{-1}$ and 2 $Å^{-1}$ arising from the mixing of antisolvent with the wet film. The major crystallographic peaks from the 3D α-phase $FASnI_3$ appear in the PEAI films after the antisolvent is dry (~3 s). As the substrate spins, the peak intensities increase due to crystal growth and extension of crystal coherence lengths by the interconnection of grains. We note that no additional peaks appear hereinafter. In the 4-FPEAI film, the same set of peaks as in the PEAI film appears promptly after injecting the antisolvent. Remarkably, we identify two additional peaks at q = 0.36 $Å^{-1}$ and 0.28 $Å^{-1}$, with onset times at 3 s and 10 s, respectively. We ascribe them to 2D TinPVK phases with n = 1 and 2.[28,32]

GIWAXS patterns of specific time frames are presented in **Figure 2d-e** for PEAI and 4-FPEAI films. For the PEAI film, the 3D α-phase $FASnI_3$ peaks appear as concentric rings when the antisolvent is dry at ~3 s spin time. The rings show relatively low intensities with no preference in azimuthal angles, and no additional phases form over the entire spin coating process. For the 4-FPEAI film, we observe the emergence of 3D α-phase $FASnI_3$ (100) peak with a strong preference at 90°, at the moment when the antisolvent hits the wet film. As the $FASnI_3$ peak intensities evolve higher over spin time, a peak at q = 0.36 $Å^{-1}$ appears at 3 s and fully grows at 10 s, which we ascribe to the (020) plane of 2D (n = 1) phase. At 10 s, following the 2D (n = 1) phase, the (020) peak of 2D (n = 2) phase at q = 0.28 $Å^{-1}$ gradually grows. The (020) peak of 2D (n = 2) becomes more prominent at 40 s, keeps increasing in intensity at 70 s and finally reaches maximum at 150 s. Moreover, a peak at q = 0.56 $Å^{-1}$ emerges at 40 s and gains in intensity over spin time, which we assign to the (040) peak of the 2D (n = 2) phase. As the high order peaks only becomes significant at long coherence lengths, this indicates the formation of multilayered 2D (n = 2) phase over spin time. To study the changes in relative intensity between the 3D and 2D phases in the 4-FPEAI films, we plotted the evolution of peak intensities against spin time in **Figure 2f** for the (100) peak of 3D α-phase $FASnI_3$, the (020) peak of 2D (n = 1) and the (020) peak of 2D (n = 2). The intensity of $FASnI_3$ (100) peak spikes at time zero and transforms to a slow growth. We also note that in the PEAI film, the $FASnI_3$ peak growth follows a similar trend as in the 4-FPEAI film, but with a lower intensity (**Figure S3**). We hypothesize that the formation of crystal grains mostly completes upon the antisolvent mixing with the wet film, and the intensity increase only originates from the enhanced crystal coherence by the attachment of adjacent grains. For the 2D phases, interestingly, the (020) peak of 2D (n = 1) picks up intensity at ~3 s following the formation of the 3D phase, reaches maximum at ~10 s of spin time, and remains unchanged for the rest of the spin coating process. In comparison, the (020) peak of 2D (n = 2), after its onset at 10 s, continues to gain intensity till the end of the spin program, surpassing the intensity of 2D (n = 1) peak at ~40 s. As most of the precursors are consumed at this stage, the 2D (n = 2) phase is unlikely to form directly. Instead, this suggests that the 2D (n = 2) phase may form at a cost of the 2D (n = 1) phase, by the diffusion of FA^+ cations and the rearrangement of $[SnI_3]_n^{n-}$ octahedra. The 2D (n = 1) phase subsequently retains its intensity as its growth balances its transformation to the 2D (n = 2) phase. In addition, the 2D (n = 2) phases do not further transform to 2D (n = 3) phases due to the high formation energy of the 2D (n = 3) phase.[33]

To investigate the crystal phase distribution in the vertical direction, we measured GIWAXS patterns of the final 4-FPEAI film at the end of the spin coating process (t = 150 s) with a range of incident angles from 0.02° to 0.9°. We plot the intensities of the (100) peak of 3D $FASnI_3$, the (020) peak of 2D (n = 1), and the (020) peak of 2D (n = 2) against the incident angles in **Figure 2g**. The line plots after background correction are displayed in **Figure S4**. The intensity profile of the 3D $FASnI_3$ peak follows a typical sigmoidal shape,

with a critical angle around 0.17°.[34-35] Both the (020) peak of 2D (n = 1) and the (020) peak of 2D (n = 2) are low in intensity below 0.2° and show drastically increased intensity at high incident angles, revealing that they both locate mainly at the bottom of the films. This distribution agrees well with the crystallization direction by the downward penetration of antisolvent injection from the top of the film, and also with the formation sequence of each phase as revealed by the in-situ GIWAXS results. We further investigate the evolution of TinPVK crystal orientations during spin coating. Azimuthal angular dependent intensities of the in-situ GIWAXS scans are plotted in **Figure 2h-i** for the $FASnI_3$ (100) peak of the PEAI and 4-FPEAI films, respectively. The raw and normalized heatmaps are displayed in **Figure S5**. We note that the indents at 65° and 115° represent the gaps between the GIWAXS detectors, as can also be seen in the GIWAXS patterns. For the PEAI film, the intensity exhibits a broad distribution among the azimuthal angles, and is relatively higher at 45° and 135°, suggesting no orientation preference. The 4-FPEAI film shows an initial broad distribution of orientations when the antisolvent is drying during the first 3 s as indicated by dash lines. As the film continues to spin, the film quickly suppresses the out-of-plane orientations, promoting a preference for 90°. In addition, the two minor peaks at 45° and 135° diminish slowly over spin time. This coincides with the morphology change we observe in the top-view SEM images.

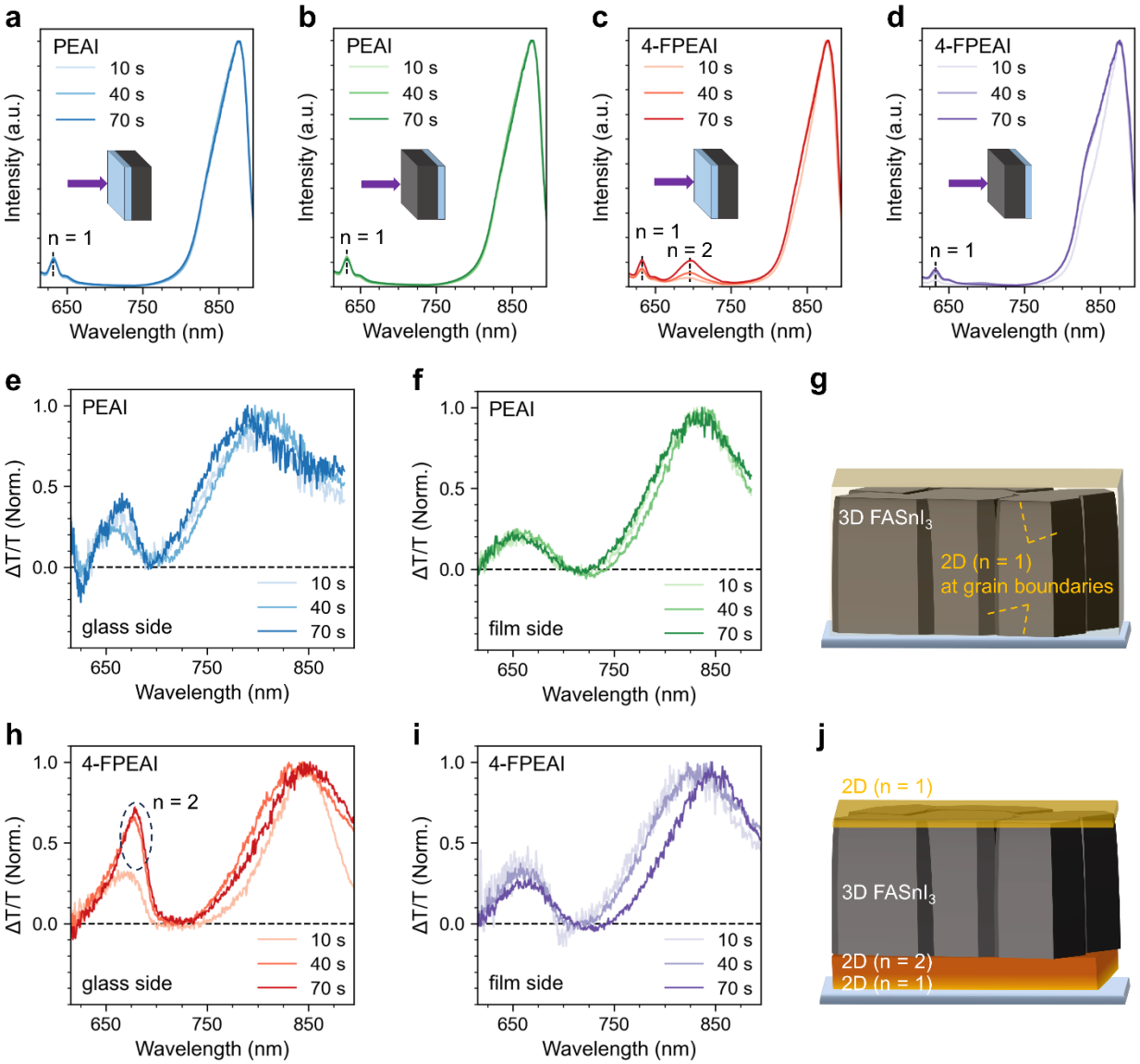

Figure 3. Heterostructures in tin perovskite films.
Steady-state photoluminescence (PL) spectra of the 10 s, 40 s, and 70 s PEAI films with the 532 nm laser excitation from (a) glass side and (b) film side. PL spectra of the 4-FPEAI films with the same excitation from (c) glass side and (d) film side. Femtosecond transient absorption (*fs*-TA) spectra (λ_{exc} = 400 nm) of the PEAI films averaged between 5-10 ps delay time with excitation from (e) glass side and (f) film side. (g)Schematic illustration of the 2D/3D heterostructure in the PEAI films. *fs*-TA spectra of the 4-FPEAI films averaged between 5-10 ps delay time with excitation from (h) glass side and (i) film side. (j) Schematic illustration of the '3D-over-2D' heterostructure in the 4-FPEAI films. All films are annealed at 70°C for 10 min after spin coating.

As the in-situ GIWAXS results reveal that crystal phases of 3D $FASnI_3$, 2D (n =1 and 2) will form at the 'pre-crystallization' stage (i.e., spin coating) in 4-FPEAI films, while only 3D $FASnI_3$ in PEAI films, we further investigate whether new 2D/3D heterostructures will form and whether 2D and 3D phase distribution will change by thermal activation at the annealing stage. We measured the steady-state photoluminescence

(PL) spectra of the TinPVK films (**Figure 3a-d**). Due to the shallow penetration depth of 532 nm laser in TinPVK films, we excited the samples from the glass side and the film side to collect PL signals from the bottom and top periphery of the TinPVK films, respectively. As shown in **Figure 3a**, the PEAI films exhibit two emission peaks from the glass side at 635 nm for 2D (n = 1) phase and at 870 nm for 3D $FASnI_3$ phase. The positions and relative intensities of the peaks do not change with longer spin times, which agrees with our findings that the consumption of precursors is fast in PEAI films and there is no structural change over the spin time. The spectra from the film side show the same set of peaks and relative intensities (**Figure 3b**), suggesting a symmetric crystal phase distribution in the vertical direction. As there are no 2D phases during the spin coating process, we hypothesize that the 2D (n = 1) phase in the PEAI films forms during annealing. Since PEAI-based 2D perovskites have relatively higher formation energies than 4-FPEAI-based counterparts,[36] external heat is needed for the formation of the PEA_2SnI_4 phase. By comparison, the 4-FPEAI films show a peak at 687 nm for 2D (n = 2) phase from the glass side in addition to the 2D (n = 1) phase and the 3D $FASnI_3$ (**Figure 3c**). Interestingly, the peak intensities of the 2D (n = 2) increases over longer spin time, with the relative intensity ratio of the other two phases unchanged. Furthermore, with the film side excitation, there is no emission from the 2D (n = 2) phase (**Figure 4d**), indicating that the 2D (n = 2) phase all concentrates at the bottom periphery of the 4-FPEAI films. These results agree well with the phase distribution extracted from the incident angle dependent GIWAXS scans (**Figure 2f**), which means the '3D-over-2D' heterostructure formed during the 'pre-crystallization' stage is preserved during annealing.

We further characterize the crystal heterostructures in TinPVK films with femtosecond transient absorption spectroscopy (*fs*-TA). The ground-state bleaching (GB) peaks of each phase caused by the band filling effect are at different wavelengths corresponding to their bandgaps, and the peak intensities are quantitative indicators for the population of each phase.[20,37] Unlike lead halide perovskites, 3D α-phase $FASnI_3$ shows two distinct GB bands that agree with two peaks in the absorption spectra, with one at the band edge and the other above the band edge, representing two accessible excited states.[22-24, 38] **Figure 3e** shows the *fs*-TA spectra of the PEAI films excited from the glass side. We ascribe the two distinct GB bands to the 3D α-phase $FASnI_3$. The *fs*-TA signal of the two GB bands shows the same decay dynamics (**Figure S6a**), following bi-exponential kinetics with τ_1 of 25 ps and τ_2 around 950 ps (**Table S1**). Unfortunately, due to the high absorption coefficient of TinPVK films, the films completely absorb the white light probe below 610 nm, blocking the signal from the 2D (n = 1) phase. For excitations from the film side, we find similar spectra shape and decay kinetics as from the glass side (**Figure 3f** and **S6b**). The spectral shapes also overlap well between different spin times. In addition, the *fs*-TA spectra averaged between 180-250 fs delay time, capturing the initial spectral response, likewise showing close agreement shapes between glass- and film-side excitation over different spin times (**Figure S7a-b**). Based on these results, we derive that the PEA ligands quickly bind to 3D $FASnI_3$ grain surfaces during spin coating, but do not form 2D phases due to the lack of thermal energy. During the annealing stage, the adsorbed PEA ligands reconstruct the $FASnI_3$ grain boundaries to form a layer of 2D (n = 1) phase as illustrated in **Figure 3g**.

In the case of 4-FPEAI, as shown in **Figure 3h**, the glass-side spectrum of the 10 s 4-FPEAI film shows two GB bands with similar spectral shape as the PEAI films. However, the 40 and 70 s films show a stronger and narrower peak at 672 nm convolved with the GB band of 3D $FASnI_3$, which we ascribe to the 2D (n = 2) phase based on its position at slightly higher energy than the 2D (n = 2) emission in **Figure 3c**. The spectra at early delay times also show this feature (**Figure S7c**), suggesting this GB band of 2D (n = 2) phase is excited by the incident laser. As displayed in **Figure S6c**, with the glass-side illumination, the *fs*-TA signal

decay dynamics of the band edge window follow bi-exponential kinetics, with τ_1 of 150 ps and τ_2 around 630 ps (**Table S2**). The decay dynamics in the high energy window exhibit tri-exponential kinetics, with the first two time constants coinciding with the band-edge window and a third component (τ_3 = 7 ns) that can be attributed to the 2D (n = 2) phase. When we illuminate from the film side, the signals from 2D (n = 2) phase disappear, leaving only the two GB bands from $FASnI_3$ (**Figure 3i** and **S7d**). The carrier decay dynamics in both wavelength windows then show bi-exponential kinetics, with time constants that agree with each other and with the corresponding time constants from the glass-side experiment (**Figure S6d** and **Table S2**). Therefore, we conclude that in the 4-FPEAI films, the '3D-over-2D' heterostructure formed during the spin coating process is well preserved during the annealing stage, as illustrated in **Figure 3j**.

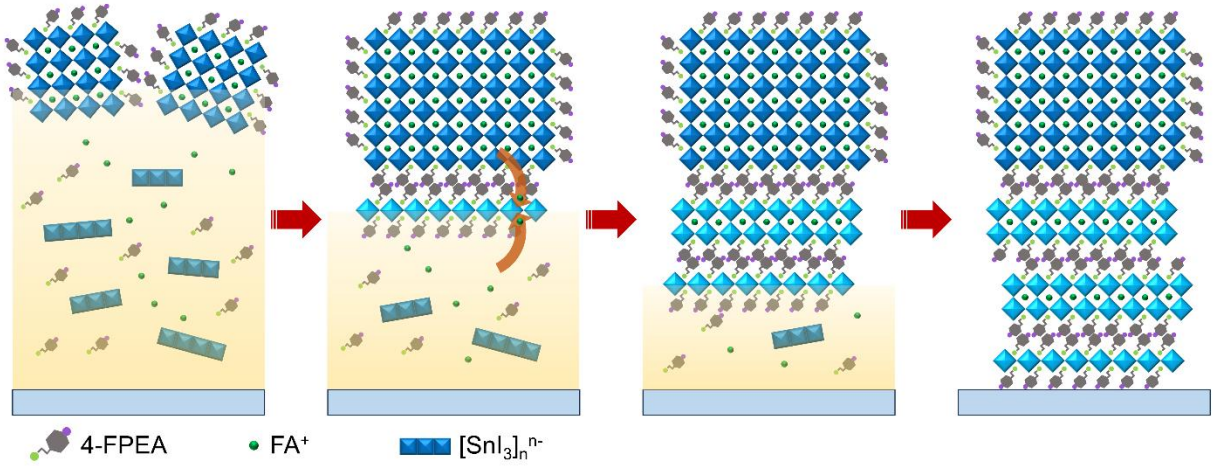

Figure 4. Proposed 'diffusion-propagation' mechanism of the '3D-over-2D' heterostructure with 4-FPEAI.

To consolidate our findings, we propose a 'diffusion-propagation' mechanism to explain the changes in crystal structures and film morphologies during the formation of the '3D-over-2D' heterostructure with 4-FPEAI (**Figure 4**). At the initial stage, when we inject the antisolvent onto the wet film, the antisolvent removes most of the solvent (DMF and DMSO) and triggers crystallization by supersaturation. Due to the limited penetration depth of the antisolvent, a trace amount of solvents remains trapped near the bottom of the wet film.[39] The majority of the 3D α-phase $FASnI_3$ is formed at this stage at the top of the film, with 4-FPEA ligands anchoring at the grain surfaces. As the solvent mixture is drying, the 3D $FASnI_3$ grains undergo self-reorientation and oriented attachment to have the {100} facet face up, manifested by the elimination of out-of-plane signal and enhanced peak intensity by the extension of crystal coherence length. Shortly after the antisolvent is dry, at ~3 s, a 2D (n = 1) monolayer forms at the bottom of the 3D $FASnI_3$. We note the $(4\text{-FPEA})_2SnI_4$ phase can form at room temperature due to a lower formation energy than $(PEA)_2SnI_4$.[36] The 2D (n = 1) phase then expand to 2D (n = 2) phase by consuming the unreacted SnI_2 species and the FA^+ cation diffused into the 2D layer.[40] At the meantime, a new 2D (n = 1) monolayer forms beneath the expanded 2D (n = 2) layer, thus conserving a consistent 2D (n = 1) phase intensity, as revealed by the in-situ GIWAXS results. We note that the TinPVK film undergoes slow lateral growth to fill up the void between grains during this stage. In addition, as the 2D sheets are parallel to the substrate, they can promote the reorientation of the crystals to be perpendicular to the substrate.[41] At longer spin time, the 2D (n = 2) phase keeps expanding to multilayers, as the GIWAXS frames show faint higher order peaks for 2D (n = 2) at above 70 s.

During the annealing stage, due to the strong interactions between 4-FPEA ligands, the diffusion of FA^+ and rearrangement of $[SnI_3]_n^{n-}$ can hardly happen further without the assistance of precursor solvent. Therefore, the prearranged '3D-over-2D' heterostructure is preserved. Crystallization mechanisms of such '3D-over-2D' heterostructures have been reported previously in lead-based perovskites by incorporating 2-aminoindan hydrochloride.[42] The large indan aromatic tails of the ligands interact strongly with PbI_2, leading to the formation of 2D sediments at the bottom of the film. In contrast, the PEAI films deplete most of the precursors promptly during antisolvent injection. The 2D (n = 1) phase cannot form without supplying external heat. Instead, the PEA ligands only attach to the grain surfaces, and transform to a layer of 2D (n =1) after annealing, resulting in a '2D-3D-mix' heterostructure with random grain orientations. There is a relatively large energy level mismatch between the conduction band minimum (CBM) of the 2D phase and 3D $FASnI_3$, but a much smaller mismatch between their valence band maximum (VBM) levels.[28] Hence, the 2D phase will impose a high energy barrier for charge transport if formed between the 3D $FASnI_3$ and the electron transport layer. However, the '3D-over-2D' heterostructure eliminates this barrier and favors the band alignment between TinPVK and hole transport layers. Subsequently, it opens up the V_{OC} and ensures efficient charge transport across the devices.

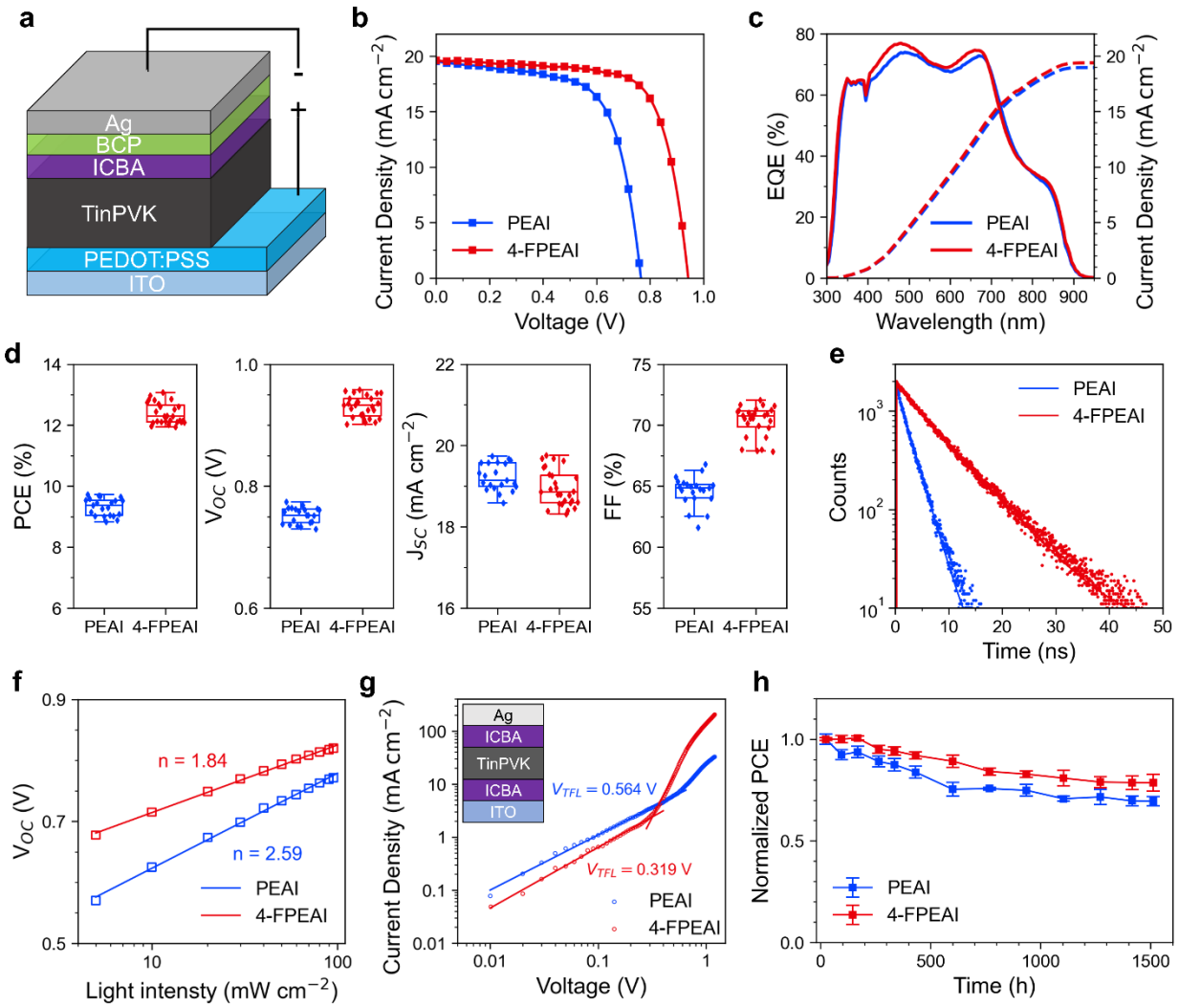

Figure 5. Photovoltaic performances of tin perovskite solar cells.
(a) Schematic illustration of the p-i-n device architecture. (b) *J-V* curves and (c) external quantum efficiency (EQE) spectra with corresponding integrated photocurrent of the best-performing devices. (d) Photovoltaic parameter statistics of the 10 s PEAI and 40 s 4-FPEAI devices. (e) Time-resolved photoluminescence (TRPL) kinetics of the 10 s PEAI and 40 s 4-FPEAI films. (f) Light intensity-dependent open-circuit voltage of the TinPSCs. (g) Space-charge-limited current (SCLC) measurements of electron-only PEAI and 4-FPEAI devices under dark conditions. (h) PCE evolution of unencapsulated PEAI and 4-FPEAI devices kept in an N_2-filled glovebox under dark.

To investigate the effect of film morphology and crystal heterostructure on photovoltaic performance, we fabricated TinPSCs with a device architecture of indium tin oxide (ITO)/poly(3,4-ethylene dioxythiophene):poly(styrene sulfonate) (PEDOT:PSS)/TinPVK/indene-C60 bisadduct (ICBA)/bathocuproine (BCP)/Ag as depicted in **Figure 5a**. Cross-sectional SEM image of a typical TinPSC is shown in **Figure S8**. The active layer is around 200-250 nm thick. The energy level alignment of the PEAI and 4-FPEAI TinPSCs is illustrated in **Figure S9** based on the 2D/3D heterostructures derived above. As mentioned above, the TinPVK films undergo lateral growth and heterostructure formation over spin time that largely affect the device performance by both pinhole elimination and band alignment. Therefore, we

vary the spin time when fabricating the TinPVK layers and summarize the photovoltaic parameters in **Figure S10-11** for PEAI and 4-FPEAI devices, respectively. The PEAI devices show the highest PCE distributions at 10 s spin time, and the performance continuously drops as the spin time increases. This mainly originates from the loss in the short circuit current density (J_{SC}). We attribute the J_{SC} loss to the randomly oriented 3D $FASnI_3$ grains and lower crystal quality after the redissolution and regrowth by the remaining solvents during spin coating. The 2D (n = 1) phase at the grain boundaries may also hinder the charge transport. Since the PEAI films all adopt '2D-3D-mix' heterostructures at any spin time, the band alignment between the TinPVK layer and the transport layers are similar, and therefore the changes in open circuit voltage (V_{OC}) are insignificant. In comparison, the 4-FPEAI devices exhibit lower PCE than the PEAI devices at 10 s spin time, owing to the low fill factor (FF). As revealed by the top-view SEM images, the incomplete surface coverage of the 10 s 4-FPEAI films can give rise to shunt channels, severely impacting the charge extraction. With 25-40 s of spin time, the 4-FPEAI films can fully cover the substrate via slow lateral growth. The device PCEs are greatly improved at 40 s of spin time, thanks to the above 70% FF and slightly improved J_{SC}. However, at longer spin time, there is a large loss in V_{OC} and minor losses in both J_{SC} and FF. As indicated by the in-situ GIWAXS results, the 2D (n = 2) phase will continue to expand into multilayered thick 2D phase over spin time. Due to the slow mobility in the out-of-plane direction of 2D TinPVK, it will inevitably limit the charge transport across the device, even though the '3D-over-2D' possesses a favorable energy alignment for p-i-n stacked solar cells. Besides, the 4-FPEAI devices may also suffer from defect formation by the redissolution and regrowth at excessively long spin times, similarly as the PEAI devices. Overall, there is an optimum spin time window for 4-FPEAI devices, which leverages the 2D phase formation, grain orientation and attachment, and crystal lateral growth.

The *J-V* curves of the best-performing devices are demonstrated in **Figure 5b**. The champion 4-FPEAI device, with 40 s spin time, achieves a PCE of 13.07% with a V_{OC} of 0.94 V, a J_{SC} of 19.62 mA cm^{-2}, and a FF of 71.1%. In contrast, the PEAI device, with 10 s spin time, produces a PCE of 9.69% with a V_{OC} of 0.76 V, a J_{SC} of 19.56 mA cm^{2}, and a FF of 65.1%. The J_{SC} of both devices are consistent with the integrated current density calculated from their external quantum efficiency (EQE) spectra (**Figure 5c**). The 4-FPEAI device only shows marginally better photon harvesting behavior in the 400-700 nm region. Statistical analysis of the 10 s PEAI and 40 s 4-FPEAI devices is summarized in **Figure 5d**. The main difference is due to higher V_{OC}, which stems from the more favorable energy alignment by the '3D-over-2D' heterostructure of the 4-FPEAI devices over the '2D-3D-mix' bulk heterostructure of the PEAI devices. Additionally, such alignment also improves the charge transport, manifested by the higher FF. Time-resolved photoluminescence (TRPL) shows a single exponential decay kinetics (**Figure 5e**), with a time constant τ of 2.33 ns and 7.18 ns for the 10 s PEAI and 40 s 4-FPEAI films, respectively. The longer decay time in the 4-FPEAI film suggests a reduced nonradiative recombination rate, which may stem from a lower bulk defect density by more controlled crystallization process with 4-FPEAI. The lower defect density in the 4-FPEAI film is also reflected in the device, as shown in the light intensity dependent V_{OC} measurements (**Figure 5f**). The V_{OC} follows the formula $ln(I)nkT/q$, where I and n are the light intensity and the diode ideality factor, respectively. The calculated ideality factors are 2.59 and 1.84 for the 10 s PEAI and 40 s 4-FPEAI devices, respectively, indicating that trap-assisted recombination is more suppressed in the 40 s 4-FPEAI device. To gain more understanding on the trap state density of the TinPVKs, we fabricated electron-only devices with a device architecture of ITO/ICBA/TinPVK/ICBA/Ag and measured the dark *J-V* curves (**Figure 5g**). The electron trap state density, N_{trap}, can be calculated with the space charge-limited current (SCLC) model: $N_{trap} = 2\varepsilon_0\varepsilon_r V_{TFL}/qL^2$, where V_{TFL} is the onset voltage of the trap-filled limit region, L is the TinPVK thickness, and ε_r of TinPVK is around 25.[43] N_{trap} is 3.22x10^{16} cm^{-3} in the 10 s PEAI device and is almost halved as 1.82x10^{16}

cm^{-3} in the 40 s 4-FPEAI device, leading to improved device performance with much lower V_{OC} deficit. The 40 s 4-FPEAI device also shows slightly better shelf stability with a T_{80} ~1200 h compared to T_{80} ~500 h for the 10 s PEAI device (**Figure 5h**). The compact packing of 4-FPEA ligands on the {100} facet eliminates higher order facets during crystallization and protects TinPVK grain surfaces against the superoxide ion (O_2^-), effectively reducing the degradation pathways.[44-45]

In conclusion, we systematically studied the ligand-assisted crystallization processes of tin perovskites with PEAI and 4-FPEAI. The PEAI films undergo fast grain formation and do not form 2D phase until the annealing stage, leading to a '2D-3D-mix' heterostructure with random grain orientation. Owing to the 'slip-on' packing mode of 4-FPEA ligands, the 4-FPEAI films form highly oriented 3D α-phase $FASnI_3$ grains with their {100} facet facing perpendicularly upwards to the substrates. In the 4-FPEAI films, 2D (n = 1) and 2D (n = 2) phases form preferably at the bottom of the films over long spin time, leading to a '3D-over-2D' heterostructure. The energy levels of the '3D-over-2D' heterostructure aligns well with the transport layers and therefore reduces the electron extraction barrier compared to the '2D-3D-mix' heterostructure. As a result, the best-performing 4-FPEAI TinPSC exhibits a significantly higher V_{OC} of 0.94 V than 0.76 V of the PEAI TinPSC, achieving a champion PCE of 13.07%. With these findings, we propose a 'diffusion-propagation' mechanism for the formation of the '3D-over-2D' heterostructure. This work deepens our understanding on tin perovskite crystallization and heterostructure formation and paves the way for high efficiency tin perovskite solar cells.

Experimental Methods

Materials

Tin powder (Sn, 99.8%), iodine (I_2, 99.99%), tin fluoride (SnF_2, 99%), hydroiodic acid (HI, 99.95%, 57 wt% in H_2O), formamidine acetate salt (FAAc, 99%), toluene (Tol, 99.8%, anhydrous), chlorobenzene (CB, 99.8%, anhydrous), isopropyl alcohol (IPA, 99.5%, anhydrous), N, N-dimethylformamide (DMF, 99.8%, anhydrous), dimethyl sulfoxide (DMSO, 99.9%, anhydrous) and bathocuproine (BCP, 99.99%) were purchased from Sigma-Aldrich. Phenethylammonium iodide (PEAI) and 4-fluorophenethylammonium iodide (4-FPEAI) were purchased from GreatCellSolar. Indene-C60 bisadduct (ICBA) was purchased from 1-Material. All chemicals were used as received without further purification.

Tin perovskite film fabrication

SnI_2 solution and FAI powder were prepared according to literature.[26] Tin perovskite precursors were prepared by mixing 19.9 mg PEAI (or 21.4 mg of 4-FPEAI), 123.8 mg FAI, 12.5 mg SnF_2 and 1 mL of 0.8 M SnI_2 solution in mixed solvent (DMF:DMSO, v:v = 4:1). The precursors were stirred at 70°C for 2 h and filtered with 0.22 μm PTFE filters before use. Tin perovskite films were deposited on substrates by spin coating at 1000 rpm for 10 s and 5000 rpm for various duration. Tol (600 μL) was cast onto the film during the second stage at the 20^{th} second. The substrates were then annealed at 70°C for 10 min to finish the crystallization.

GIWAXS measurements

Grazing-incident wide-angle X-ray scattering (GIWAXS) measurements were conducted in the Complex Materials Scattering (CMS, 11-BM) beamline of the National Synchrotron Light Source II (NSLS-II) at Brookhaven National Laboratory. The in-situ GIWAXS measurements employed a home-built spin coater stage (**Figure S2**). TinPVK precursor was loaded onto PEDOT:PSS coated glass substrates before the start of the measurements. A spin program of 1000 rpm for 10 s then 5000 rpm for 170 s was used. Antisolvent

(Tol) was discharged onto the spinning substrate at the 20th second of the second stage with a remotely controlled syringe pump. A metal cover was used to enclose the spin coater chamber and a constant N_2 flow was used to create an inert atmosphere. The X-ray beam had a size of 200 µm (horizontally) × 50 µm (vertically), a divergence of 1 mrad and an energy of 13.5 keV with a resolution of 0.7%. The scattered data were collected with a customized Pilatus 800K area detector (Dectris, Switzerland), which consists of 0.172 mm square pixels in a 1043 × 981 array, placed ~ 0.260 meters downstream from the sample position. The in-situ GIWAXS data was acquired with a frame rate of 5 frames/s, and the incident angle was kept constant at 0.9° throughout the data acquisition process. After each in-situ measurements, the sample was measured at a range of incident angles from 0.02° to 0.9° with an exposure time of 2 s to study the distribution of phases at different depth. The collected 2D scattering patterns were analyzed by a Python package provided by the beamline staff.

Film characterization

Top-view and cross-sectional scanning electron microscope (SEM) images were acquired using a Zeiss Gemini-500 FESEM operated at 2 kV. X-ray diffraction patterns were collected using a Bruker-D8-Powder-Diffractometer. Time-resolved photoluminescence (TRPL) spectra were measured using an Edinburgh FLS1000 Spectrometer. Steady-state PL spectra were collected using subnanosecond pulsed laser (Picolo MOPA, InnoLas) and ICCD detector (PI-MAX4, Princeton Instruments). Transient absorption measurements were conducted with an automated transient absorption spectrometer (HELIOS, Ultrafast Systems), driven by a Yb:KGW amplifier (PHAROS-SP, Light Conversion) operating at 8 kHz. An optical parametric amplifier (OPA) and its second harmonic (SH) module (ORPHEUS and LYRA-SH, Light Conversion), pumped by a Yb:KGW amplifier (PHAROS-SP, Light Conversion) generates a 200-fs narrowband pump pulse. A portion of the fundamental was separated to generate a white light continuum probe pulse ranging from 2.53 to 1.35 eV using a 1 cm YAG crystal. The beam diameters (1/e2 height) for pump and probe pulses at the sample position were 650 and 75 µm, respectively. TA spectra were collected with magic angle condition between pump and probe and in a shot-to-shot fashion. Pump-probe time delay was set by a mechanical delay stage from -3 to 7000 ps.

Device fabrication and testing

ITO coated glass substrates were cleaned by sequential sonication in soapy water, DI water, acetone, and IPA for 15 min each. The cleaned substrates were treated with oxygen plasma at 45 W for 15 min before spin coating. PEDOT:PSS (Clevios Al 4083) was filtered by 0.45 µm Nylon filter and spin coated onto the substrates at 5000 rpm for 40 s. The substrates were then annealed at 150 °C for 20 min. Tin perovskite films were deposited onto the PEDOT:PSS layer as described above. Next, ICBA (20 mg/mL in CB) was spin coated onto the tin perovskite layers at 1000 rpm for 30 s and annealed at 70 °C for 10 min. BCP (0.5 mg/mL in IPA) was spin coated at 6000 rpm for 30 s. Finally, 100 nm Ag back electrodes were deposited under a vacuum of $<10^{-7}$ torr. The electron-only devices were fabricated with a device architecture of ITO/ICBA/TinPVK/ICBA/Ag. The photocurrent density–voltage (*J*–*V*) sweeps were recorded in a N_2-filled glovebox with a SS-F5-3A Solar Simulator (EnliTech). Before the measurements, the light intensity was calibrated to 100 mW cm^2 using a standardized National Renewable Energy Laboratory calibrated silicon solar cell. An opening area of 0.0324 cm^2 was defined by a shadow mask during the measurements. The external quantum efficiency spectra were recorded with a QE-RX system (EnliTech).

SUPPORTING INFORMATION

Supporting Information Available: <peak width analysis of XRD spectra; schematic illustrations of the in-situ GIWAXS setup; evolutions of in-situ GIWAXS peak intensity; Incident angle dependent GIWAXS linecuts; evolutions of crystal orientations; *fs*-TA decay dynamics and fitted time constants; *fs*-TA spectra at early delay times; cross-sectional SEM image of a typical device; energy level alignment of TinPSCs; photovoltaic parameters of PEAI and 4-FPEAI devices with different spin times.>

Acknowledgements

This work is financially supported by NSF ECCS-2054942. This work makes use of the Cornell Center for Materials Research shared facilities under NSF MRSEC program DMR-1719875. A.J.M. and J.K. were supported by the U.S. Department of Energy, Office of Science, Basic Energy Sciences, CPIMS Program under Early Career Research Program (Award No. DE-SC0021941). J.K. was supported by Basic Science Research Program through the National Research Foundation of Korea (NRF) funded by the Ministry of Education (2022R1A6A3A03072477). The GIWAXS experiments use resources at the Centre for Functional Nanomaterials and the CMS beamline (11-BM) of the National Synchrotron Light Source II (NSLS-II), both supported by U.S. DOE Office of Science Facilities at Brookhaven National Laboratory under Contract No. DE-SC0012704.

Author contributions

Y.X. and Q.Y. conceived the idea. Y.X. designed the experiments and drafted the manuscript. Y.X. fabricated the TinPVK films and measured XRD and SEM; Y.X. and S.R. conducted the GIWAXS measurements, with the help form Y.Z. at 11-BM of NSLS-II; Y.X. and J.K. carried out static PL and *fs*-TA measurements and analyzed the data with the help of A.J.M.; Y.X., T.C. and X.Z. fabricated and tested TinPSCs. All authors discussed the results and commented on the manuscript.

Competing interests

The authors declare no competing interests.

References

(1) *Best Research-Cell Efficiency Chart (date of access: 7/27/2024).* https://www.nrel.gov/pv/cell-efficiency.html

(2) Zhu, P.; Chen, C.; Dai, J.; Zhang, Y.; Mao, R.; Chen, S.; Huang, J.; Zhu, J. Toward the Commercialization of Perovskite Solar Modules. *Advanced Materials* **2024**, *36* (15), 2307357.

(3) Li, N.; Niu, X.; Chen, Q.; Zhou, H. Towards commercialization: the operational stability of perovskite solar cells. *Chemical Society Reviews* **2020**, *49* (22), 8235-8286.

(4) Chen, C. H.; Cheng, S. N.; Cheng, L.; Wang, Z. K.; Liao, L. S. Toxicity, leakage, and recycling of lead in perovskite photovoltaics. *Advanced energy materials* **2023**, *13* (14), 2204144.

(5) Ren, M.; Qian, X.; Chen, Y.; Wang, T.; Zhao, Y. Potential lead toxicity and leakage issues on lead halide perovskite photovoltaics. *Journal of Hazardous Materials* **2022**, *426*, 127848.

(6) Li, J.; Cao, H.-L.; Jiao, W.-B.; Wang, Q.; Wei, M.; Cantone, I.; Lü, J.; Abate, A. Biological impact of lead from halide perovskites reveals the risk of introducing a safe threshold. *Nature communications* **2020**, *11* (1), 310.

(7) Yang, M.; Tian, T.; Fang, Y.; Li, W.-G.; Liu, G.; Feng, W.; Xu, M.; Wu, W.-Q. Reducing lead toxicity of perovskite solar cells with a built-in supramolecular complex. *Nature Sustainability* **2023**, *6* (11), 1455-1464.

(8) Li, X.; Zhang, F.; Wang, J.; Tong, J.; Xu, T.; Zhu, K. On-device lead-absorbing tapes for sustainable perovskite solar cells. *Nature Sustainability* **2021**, *4* (12), 1038-1041.

(9) Park, S. Y.; Park, J.-S.; Kim, B. J.; Lee, H.; Walsh, A.; Zhu, K.; Kim, D. H.; Jung, H. S. Sustainable lead management in halide perovskite solar cells. *Nature Sustainability* **2020**, *3* (12), 1044-1051.

(10) Jiang, X.; Zang, Z.; Zhou, Y.; Li, H.; Wei, Q.; Ning, Z. Tin halide perovskite solar cells: an emerging thin-film photovoltaic technology. *Accounts of Materials Research* **2021**, *2* (4), 210-219.

(11) López-Fernández, I.; Valli, D.; Wang, C. Y.; Samanta, S.; Okamoto, T.; Huang, Y. T.; Sun, K.; Liu, Y.; Chirvony, V. S.; Patra, A. Lead-Free Halide Perovskite Materials and Optoelectronic Devices: Progress and Prospective. *Advanced Functional Materials* **2024**, *34* (6), 2307896.

(12) Liu, H.; Zhang, Z.; Zuo, W.; Roy, R.; Li, M.; Byranvand, M. M.; Saliba, M. Pure tin halide perovskite solar cells: focusing on preparation and strategies. *Advanced Energy Materials* **2023**, *13* (3), 2202209.

(13) Liu, J.; Yao, H.; Wang, S.; Wu, C.; Ding, L.; Hao, F. Origins and suppression of Sn (II)/Sn (IV) oxidation in tin halide perovskite solar cells. *Advanced Energy Materials* **2023**, *13* (23), 2300696.

(14) Zhang, Z.; Huang, Y.; Jin, J.; Jiang, Y.; Xu, Y.; Zhu, J.; Zhao, D. Mechanistic Understanding of Oxidation of Tin-based Perovskite Solar Cells and Mitigation Strategies. *Angewandte Chemie* **2023**, *135* (45), e202308093.

(15) Dong, H.; Ran, C.; Gao, W.; Sun, N.; Liu, X.; Xia, Y.; Chen, Y.; Huang, W. Crystallization dynamics of Sn-based perovskite thin films: toward efficient and stable photovoltaic devices. *Advanced Energy Materials* **2022**, *12* (1), 2102213.

(16) Chen, J.; Luo, J.; Hou, E.; Song, P.; Li, Y.; Sun, C.; Feng, W.; Cheng, S.; Zhang, H.; Xie, L. Efficient tin-based perovskite solar cells with trans-isomeric fulleropyrrolidine additives. *Nature Photonics* **2024**, 18, 464–470.

(17) Shi, Y.; Zhu, Z.; Miao, D.; Ding, Y.; Mi, Q. Interfacial Dipoles Boost Open-Circuit Voltage of Tin Halide Perovskite Solar Cells. *ACS Energy Letters* **2024**, *9*, 1895-1897.

(18) Shao, S.; Liu, J.; Portale, G.; Fang, H. H.; Blake, G. R.; ten Brink, G. H.; Koster, L. J. A.; Loi, M. A. Highly reproducible Sn-based hybrid perovskite solar cells with 9% efficiency. *Advanced Energy Materials* **2018**, *8* (4), 1702019.

(19) Wang, J.; Yang, C.; Chen, H.; Lv, M.; Liu, T.; Chen, H.; Xue, D.-J.; Hu, J.-S.; Han, L.; Yang, S. Oriented attachment of tin halide perovskites for photovoltaic applications. *ACS Energy Letters* **2023**, *8* (3), 1590-1596.
(20) Li, H.; Xu, Y.; Ramakrishnan, S.; Zhang, Y.; Cotlet, M.; Xu, T. L.; Yu, Q. Pseudo-halide anion engineering for efficient quasi-2D Ruddlesden-Popper tin perovskite solar cells. *Cell Reports Physical Science* **2022**, *3* (10), 101060.
(21) Jiang, X.; Wang, F.; Wei, Q.; Li, H.; Shang, Y.; Zhou, W.; Wang, C.; Cheng, P.; Chen, Q.; Chen, L. Ultra-high open-circuit voltage of tin perovskite solar cells via an electron transporting layer design. *Nature communications* **2020**, *11* (1), 1245.
(22) Liao, Y.; Liu, H.; Zhou, W.; Yang, D.; Shang, Y.; Shi, Z.; Li, B.; Jiang, X.; Zhang, L.; Quan, L. N. Highly oriented low-dimensional tin halide perovskites with enhanced stability and photovoltaic performance. *Journal of the American Chemical Society* **2017**, *139* (19), 6693-6699.
(23) Wang, F.; Jiang, X.; Chen, H.; Shang, Y.; Liu, H.; Wei, J.; Zhou, W.; He, H.; Liu, W.; Ning, Z. 2D-quasi-2D-3D hierarchy structure for tin perovskite solar cells with enhanced efficiency and stability. *Joule* **2018**, *2* (12), 2732-2743.
(24) Zhao, J.; Zhang, Z.; Li, G.; Aldamasy, M. H.; Li, M.; Abate, A. Dimensional tuning in lead-free Tin Halide perovskite for solar cells. *Advanced Energy Materials* **2023**, *13* (13), 2204233.
(25) Yu, B. B.; Chen, Z.; Zhu, Y.; Wang, Y.; Han, B.; Chen, G.; Zhang, X.; Du, Z.; He, Z. Heterogeneous 2D/3D tin-halides perovskite solar cells with certified conversion efficiency breaking 14%. *Advanced Materials* **2021**, *33* (36), 2102055.
(26) Zhang, F.; Kim, D. H.; Lu, H.; Park, J.-S.; Larson, B. W.; Hu, J.; Gao, L.; Xiao, C.; Reid, O. G.; Chen, X. Enhanced charge transport in 2D perovskites via fluorination of organic cation. *Journal of the American Chemical Society* **2019**, *141* (14), 5972-5979.
(27) Yan, L.; Ma, J.; Li, P.; Zang, S.; Han, L.; Zhang, Y.; Song, Y. Charge-carrier transport in quasi-2D Ruddlesden–Popper perovskite solar cells. *Advanced Materials* **2022**, *34* (7), 2106822.
(28) Wang, T.; Loi, H. L.; Cao, J.; Qin, Z.; Guan, Z.; Xu, Y.; Cheng, H.; Li, M. G.; Lee, C. S.; Lu, X. High Open Circuit Voltage Over 1 V Achieved in Tin-Based Perovskite Solar Cells with a 2D/3D Vertical Heterojunction. *Advanced Science* **2022**, *9* (18), 2200242.
(29) Yao, H.; Wu, T.; Xiao, Y.; Ding, L.; Hua, Y.; Hao, F. Regulating the Crystallization and Carrier Dynamics for High-Performance Quasi-2D Tin Perovskite Solar Cells. *ACS Materials Letters* **2023**, *5*, 3203-3211.
(30) Zhu, L.; Yuh, B.; Schoen, S.; Li, X.; Aldighaithir, M.; Richardson, B. J.; Alamer, A.; Yu, Q. Solvent-molecule-mediated manipulation of crystalline grains for efficient planar binary lead and tin triiodide perovskite solar cells. *Nanoscale* **2016**, *8* (14), 7621-7630.
(31) Jiang, X.; Li, H.; Zhou, Q.; Wei, Q.; Wei, M.; Jiang, L.; Wang, Z.; Peng, Z.; Wang, F.; Zang, Z. One-step synthesis of SnI2·(DMSO) x adducts for high-performance tin perovskite solar cells. *Journal of the American Chemical Society* **2021**, *143* (29), 10970-10976.
(32) Min, H.; Wang, N.; Chen, N.; Tong, Y.; Wang, Y.; Wang, J.; Liu, J.; Wang, S.; Wu, X.; Yang, P. Spin coating epitaxial heterodimensional tin perovskites for light-emitting diodes. *Nature Nanotechnology* **2024**, 1-6.
(33) Milić, J. V.; Zakeeruddin, S. M.; Grätzel, M. Layered hybrid formamidinium lead iodide perovskites: challenges and opportunities. *Accounts of Chemical Research* **2021**, *54* (12), 2729-2740.
(34) Dong, J.; Shao, S.; Kahmann, S.; Rommens, A. J.; Hermida-Merino, D.; ten Brink, G. H.; Loi, M. A.; Portale, G. Mechanism of crystal formation in Ruddlesden–Popper Sn-based perovskites. *Advanced Functional Materials* **2020**, *30* (24), 2001294.
(35) Hoffman, J. M.; Strzalka, J.; Flanders, N. C.; Hadar, I.; Cuthriell, S. A.; Zhang, Q.; Schaller, R. D.; Dichtel, W. R.; Chen, L. X.; Kanatzidis, M. G. In situ grazing-incidence wide-angle scattering reveals mechanisms for phase distribution and disorientation in 2D halide perovskite films. *Advanced Materials* **2020**, *32* (33), 2002812.

(36) Hu, J.; Oswald, I. W.; Stuard, S. J.; Nahid, M. M.; Zhou, N.; Williams, O. F.; Guo, Z.; Yan, L.; Hu, H.; Chen, Z. Synthetic control over orientational degeneracy of spacer cations enhances solar cell efficiency in two-dimensional perovskites. *Nature communications* **2019**, *10* (1), 1276.
(37) Ramakrishnan, S.; Li, H.; Xu, Y.; Shin, D.; Dursun, I.; Cotlet, M.; Zhang, Y.; Yu, Q. Ruddlesden–Popper Perovskites with Narrow Phase Distribution for Air-Stable Solar Cells. *Solar RRL* **2022**, *6* (9), 2200490.
(38) Dai, L.; Deng, Z.; Auras, F.; Goodwin, H.; Zhang, Z.; Walmsley, J. C.; Bristowe, P. D.; Deschler, F.; Greenham, N. C. Slow carrier relaxation in tin-based perovskite nanocrystals. *Nature Photonics* **2021**, *15* (9), 696-702.
(39) Chen, S.; Dai, X.; Xu, S.; Jiao, H.; Zhao, L.; Huang, J. Stabilizing perovskite-substrate interfaces for high-performance perovskite modules. *Science* **2021**, *373* (6557), 902-907.
(40) Ramakrishnan, S.; Song, D.; Xu, Y.; Zhang, X.; Aksoy, G.; Cotlet, M.; Li, M.; Zhang, Y.; Yu, Q. Solvent-Mediated Formation of Quasi-2D Dion-Jacobson Phases on 3D Perovskites for Inverted Solar Cells Over 23% Efficiency. *Advanced Energy Materials* **2023**, *13* (45), 2302240.
(41) Li, H.; Zang, Z.; Wei, Q.; Jiang, X.; Ma, M.; Xing, Z.; Wang, J.; Yu, D.; Wang, F.; Zhou, W. High-member low-dimensional Sn-based perovskite solar cells. *Science China Chemistry* **2023**, *66* (2), 459-465.
(42) Li, H.; Zhang, C.; Gong, C.; Zhang, D.; Zhang, H.; Zhuang, Q.; Yu, X.; Gong, S.; Chen, X.; Yang, J. 2D/3D heterojunction engineering at the buried interface towards high-performance inverted methylammonium-free perovskite solar cells. *Nature Energy* **2023**, *8* (9), 946-955.
(43) Qiu, J.; Xia, Y.; Chen, Y.; Huang, W. Management of crystallization kinetics for efficient and stable low-dimensional Ruddlesden–Popper (LDRP) lead-free perovskite solar cells. *Advanced Science* **2019**, *6* (1), 1800793.
(44) Slavney, A. H.; Smaha, R. W.; Smith, I. C.; Jaffe, A.; Umeyama, D.; Karunadasa, H. I. Chemical approaches to addressing the instability and toxicity of lead–halide perovskite absorbers. *Inorganic chemistry* **2017**, *56* (1), 46-55.
(45) Triggs, C. T.; Ross, R. D.; Mihalyi-Koch, W.; Clewett, C. F.; Sanders, K. M.; Guzei, I. A.; Jin, S. Spacer Cation Design Motifs for Enhanced Air Stability in Lead-Free 2D Tin Halide Perovskites. *ACS Energy Letters* **2024**, *9* (4), 1835-1843.